JCI The Journal of Clinical Investigation

Mitochondrial dysfunction reactivates α-fetoprotein expression that drives copper-dependent immunosuppression in mitochondrial disease models

Kimberly A. Jett, … , Vishal M. Gohil, Scot C. Leary

J Clin Invest. 2022. https://doi.org/10.1172/JCI154684.

Research In-Press Preview **Metabolism**

Graphical abstract

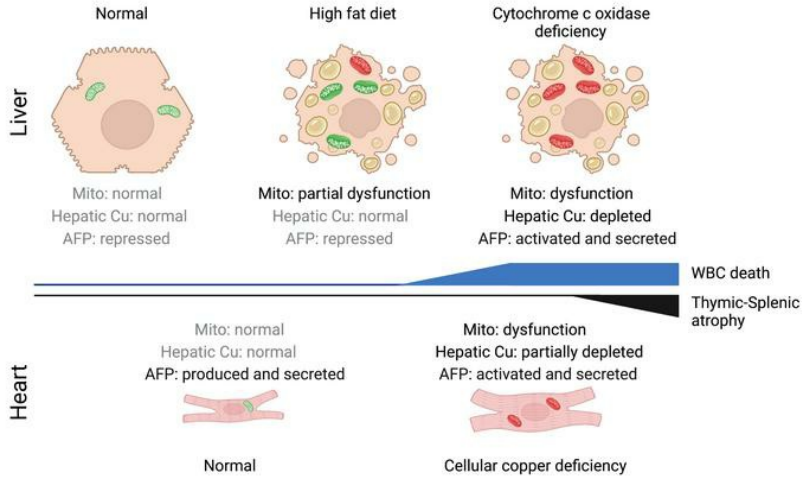

Find the latest version:

https://jci.me/154684/pdf

Mitochondrial dysfunction reactivates α-fetoprotein expression that drives copper-dependent immunosuppression in mitochondrial disease models

Kimberly A. Jett[1], Zakery N. Baker[1], Amzad Hossain[1], Aren Boulet[1], Paul A. Cobine[2], Sagnika Ghosh[3], Philip Ng[4], Orhan Yilmaz[1], Kris Barreto[5], John DeCoteau[5], Karen Mochoruk[5], George N. Ioannou[6,7,8], Christopher Savard[6,7,8], Sai Yuan[9], Osama H.M.H. Abdalla[10,11], Christopher Lowden[10,11], Byung-Eun Kim[9], Hai-Ying Mary Cheng[10,11], Brendan J. Battersby[12], Vishal M. Gohil[3] and Scot C. Leary[1,*]

[1]Department of Biochemistry, Microbiology and Immunology, University of Saskatchewan, Saskatoon, SK S7N 5E5, Canada

[2]Department of Biological Sciences, Auburn University, Auburn, AL, USA

[3]Department of Biochemistry and Biophysics, Texas A&M University, College Station, TX, USA

[4]Molecular and Human Genetics, Baylor College of Medicine, Houston, USA

[5]Department of Laboratory and Pathology Medicine, University of Saskatchewan, Saskatoon, SK S7N 5E5, Canada

[6]Division of Gastroenterology and [7]Research and Development, Veterans Affairs Puget Sound Health Care System and the [8]Division of Gastroenterology, Department of Medicine, University of Washington, Seattle, USA

[9]Department of Animal and Avian Sciences, University of Maryland, Maryland, MD, USA

[10]Department of Biology, University of Toronto Mississauga, Mississauga, ON, Canada

[11]Department of Cell and Systems Biology, University of Toronto, Toronto, ON M5S 3G5, Canada

[12] Institute of Biotechnology, University of Helsinki, Helsinki, Finland

[*]Correspondence to: Dr. Scot C. Leary
BMI, University of Saskatchewan
107 Wiggins Rd, Health Sciences Building Rm 4D01.7
Saskatoon, SK S7N 5E5
Phone: 3069664349
Email: scot.leary@usask.ca

Abstract

Signaling circuits crucial to systemic physiology are widespread, yet uncovering their molecular underpinnings remains a barrier to understanding the etiology of many metabolic disorders. Here, we identified a copper-linked signaling circuit activated by disruption of mitochondrial function in the murine liver or heart that resulted in atrophy of the spleen and thymus and caused a peripheral white blood cell deficiency. We demonstrated that the leukopenia was caused by α-fetoprotein, which required copper and the cell surface receptor CCR5 to promote white blood cell death. We further showed that α-fetoprotein expression was upregulated in several cell types upon inhibition of oxidative phosphorylation. Collectively, our data argue that α-fetoprotein may be secreted by bioenergetically stressed tissue to suppress the immune system, an effect which may explain the recurrent or chronic infections that are observed in a subset of mitochondrial diseases or in other disorders with secondary mitochondrial dysfunction.

Introduction

To maintain homeostasis, tissue and organ systems must adapt in unison to varying metabolic challenges (1). These responses involve a cell autonomous component that acts locally at the affected tissue and a complementary, cell non-autonomous component in which secreted factors communicate with other tissues to allow for a coherent systemic response (2, 3). Therefore, to gain insights into systemic physiology and disease etiology it is imperative that we understand how organs sense their functional state and communicate it to distal tissues (4, 5).

A defining feature of human mitochondrial disorders is their tremendous clinical heterogeneity with variable tissue-specificity, onset and severity (6). While the importance of oxidative phosphorylation (OXPHOS) to cell fitness is widely recognized, the cell and tissue-specific consequences of the mitochondrial dysregulation that leads to the activation of cellular stress responses that ultimately contribute to disease pathogenesis remain poorly characterized. Therefore, a thorough understanding of these molecular mechanisms and how they contribute to pathogenesis is required. Over the last decade, a compendium of studies in human patients and model organisms points to mitochondrial dysfunction as a potent inducer of the integrated stress response (ISR) (7). The ISR is an evolutionarily conserved, intracellular signaling cascade that finely tunes cytoplasmic protein synthesis and nuclear gene expression to preserve homeostasis in response to cellular stress (7). Activating transcription factor 4 (ATF4) integrates the four branches of the ISR, directing the expression and secretion of a number of factors. Two of these branches require the translation initiation factors GCN2 and HRI, and each has been shown to communicate mitochondrial dysfunction (8-10). In the context of OXPHOS defects, the enhanced secretion of GDF15 and FGF21 remodels metabolism and both growth factors are recognized as robust biomarkers for mitochondrial disorders (11). However, whether the ISR

plays a general role in modulating clinically relevant phenotypes in the molecular pathogenesis of mitochondrial disease remains an outstanding question in the field.

The interplay between mitochondrial dysfunction and the immune system in disease pathogenesis is also poorly understood (12-14), yet patients can present with neutropenia or pancytopenia (15, 16). A comprehensive study investigating immune function and risk of infection further showed that patients with mitochondrial disease had a higher risk of suffering from recurrent infections (17). Here, we establish that an isolated deficiency in cytochrome *c* oxidase (COX) in the liver or heart triggers the secretion of α-fetoprotein (AFP), which then acts systemically to suppress the peripheral immune system by inducing the death of white blood cells (WBCs). AFP therefore appears to play a hitherto underappreciated role in immunomodulatory responses to bioenergetic stress that impact systemic physiology and may contribute significantly to disease progression in patients with mitochondrial disorders who suffer from recurrent infections.

Results

Hepatocyte-specific deletion of Sco1 triggers a progressive leukopenia and atrophy of the thymus and spleen

We previously demonstrated that mice lacking the copper chaperone *Sco1* in hepatocytes (*Sco1*^{hep}) develop normally during the first month of life, but subsequently fail to thrive and have a median life expectancy of 70 days (18). Surprisingly, adult *Sco1*^{hep} mice exhibit a severe leukopenia and profound atrophy of the spleen (18); however, it is unclear whether these phenotypes are a direct consequence of ablating *Sco1* expression in hepatocytes or a secondary consequence of liver failure. Therefore, to understand if hepatic deletion of *Sco1* triggers systemic signalling that affects cells and organs of the immune system, we measured complete

blood cell (CBC) counts, quantified organ mass and examined the ultrastructure of the thymus in *Sco1*^{hep} mice and age-matched littermate controls at post-natal day 18, 27, 37 and 47 (Figure 1). This sampling schedule was selected because at post-natal day 27 (P27) *Sco1*^{hep} mice are outwardly indistinguishable from *Control* littermates yet their livers already exhibit a severe, combined COX and copper deficiency (18). We found that the WBC count deficiency in terminal blood drawn from *Sco1*^{hep} mice was already manifest at P27 and progressively worsened thereafter (Figure 1A). Notably, we did not detect any changes in red blood cell (RBC) counts (Figure 1A). The onset of the leukopenia preceded any loss in body weight and was ultimately accompanied by the disproportionate atrophy of the spleen and thymus relative to other organs (Figure 1B). These data suggest that the effects on the peripheral immune system in *Sco1*^{hep} mice are not secondary to liver failure, and clearly establish that the leukopenia is manifest prior to the atrophy of the thymus and spleen.

To gain further insight into the underlying atrophy of the thymus, we examined thymic ultrastructure using standard hematoxylin and eosin (H&E) staining (Figure 1C). While the thymi of *Control* and *Sco1*^{hep} mice are similar at P27, histological analysis of the P37 *Sco1*^{hep} thymus revealed a selective thinning of the cortex (Figure 1C) and the presence of tingible body macrophages (Figure S1A). Additional atrophy at P47 was accompanied by a further reduction in the ratio of cortex to medulla, disruption of the cortical-medullary boundary and increased vascularity (Figures 1C, S1A). These data together with our previous findings (18) suggest that loss of *Sco1* function in hepatocytes has a profound effect on the peripheral immune system, and that atrophy of the thymus and spleen in *Sco1*^{hep} mice ultimately contributes to the progressive severity of the leukopenia.

The liver secretes an immunosuppressive factor in response to bioenergetic stress caused by mitochondrial dysfunction

While characterization of the albumin Cre recombinase driver we used for *Sco1* deletion has demonstrated that loxP mediated gene excision is largely restricted to hepatocytes (19), we wanted to ensure that the observed immune phenotypes are indeed directly attributable to the loss of SCO1 function in the liver. We therefore sought to restore *Sco1* expression in the liver of *Sco1*^{hep} mice using a helper-dependent adenoviral approach (20, 21). After establishing that intracardiac administration was superior to intraperitoneal injection for specific delivery of helper-dependent adenovirus to the liver relative to other peripheral organs (Figure S1B), we injected 21-24 day old *Sco1*^{hep} mice and *Control* littermates with vehicle or a helper-dependent adenovirus containing a *Sco1* cDNA under the control of a liver-specific PEPCK promoter. SCO1 abundance was significantly increased in the livers of both *Control* and *Sco1*^{hep} mice (Figure 1D), which rescued the copper deficiency and the levels of the cellular copper importer CTR1 (Figure S1C, D). Zinc and iron levels were also normalized in the livers of *Sco1*^{hep} mice injected with adenovirus (Figure S1C). Critically, adenovirus administration normalized body and organ weights and restored WBC counts in *Sco1*^{hep} mice (Figure 1E, F). These data show that the immunosuppressive effects of *Sco1* loss-of-function are specific to its role in hepatocytes and not attributable to aberrant Cre recombinase expression in other cell types.

To determine if the immunosuppressive effect we observe is unique to the *Sco1*^{hep} mouse model, we generated two additional hepatocyte-specific knockout lines that lacked the COX assembly factor *Coa5* or *Cox10*. Unlike *Sco1*^{hep} mice, and in agreement with existing literature, hepatocyte-specific deletion of *Coa5* or *Cox10* (22) was not lethal (Figure S2A,B). Therefore, *Coa5*^{hep} and *Cox10*^{hep} mice were sampled at P77 and P64, respectively, as they display the

greatest body weight difference at these time points when compared to *Control* littermates (Figure S2A, B). Both *Coa5*^{hep} (Figure S2C) and *Cox10*^{hep} (18) mice exhibited a severe, combined COX and copper deficiency in the liver, and a significant leukopenia in the absence of changes in RBC counts (Figure 2A, B). Copper levels in the circulation were higher in both *hep* models (Figure S2D), while atrophy of the thymus and spleen was marked in *Coa5*^{hep} mice and relatively modest in *Cox10*^{hep} animals (Figure 2C).

To evaluate whether the varying severity of the leukopenia we observe across our mouse models is attributable to differences in hepatic bioenergetic status, we next quantified total ATP levels in age-matched *Control* and *hep* livers and plotted them against total WBC counts. These analyses revealed a significant, positive correlation between hepatic ATP content and WBC counts (Figure 2D). Consistent with the idea that perturbed energy homeostasis is associated with mitochondrial dysfunction, *Sco1*^{hep} and *Cox10*^{hep} livers exhibit a significant increase in the abundance of the phosphorylated form of eIF2α, a key player in the ISR (23, 24) (Figure 2E). Given that the ISR is a robust intracellular signaling cascade that can integrate both endoplasmic reticulum (ER) and mitochondrial dysfunction (Costal-Mattioli and Walter, 2020), we also quantified the transcript abundance of ATF6, a well-known transcription factor that is activated upon ER stress, and found that it was up-regulated in the *hep* livers of both the *Sco1* and *Cox10* mouse models (Figure 2F).

Taken together, our findings from three unique mouse models argue that ER stress and mitochondrial dysfunction in the liver triggers the secretion of a factor that suppresses the peripheral immune system. Our data further suggest that the severity of the leukopenia is a direct reflection of the extent to which the *hep* liver is bioenergetically stressed as a result of impaired mitochondrial function.

Hepatic mitochondrial dysfunction leads to the secretion of the immunosuppressive factor AFP

To establish that a secreted factor is responsible for the immune phenotypes we observe as a result of mitochondrial dysfunction in the liver, we serially administered *Control* or *Sco1*^{hep} plasma to 21-24 day old *Control* mice over 28 days via tail vein injection. Mice injected with *Sco1*^{hep} plasma exhibited a significant leukopenia relative to those injected with *Control* plasma (Figure 3A) independent of alterations in thymic mass (Figure S3A), emphasizing that the leukopenia in our *hep* models does not require atrophy of the spleen or thymus. Taken together, these findings are consistent with a model whereby the *Sco1*^{hep} liver is secreting a factor into the blood that is suppressing the peripheral immune system.

A number of secreted molecules including proteins, lipids, nucleic acids and metabolites could account for the observed immune phenotypes (25, 26). To distinguish between these possibilities, we performed an *in vitro* primary blood mononuclear cell (PBMC) viability assay with *Control* and *hep* plasma sources. PBMCs grown in RPMI containing *Control* plasma are indistinguishable from those grown in media supplemented with fetal bovine serum (Figures 3B, S3D; - vs *Control*). In contrast, the viability of PBMCs co-cultured with *Sco1*^{hep} or *Cox10*^{hep} plasma was significantly diminished (Figure 3B). Because *Sco1*^{hep} livers have profound alterations in lipid metabolism reminiscent of non-alcoholic fatty liver disease (NAFLD) (18), we next addressed the possibility that the observed effects in PBMC cultures were attributable to one or more lipid species. We found that PBMC viability was unaffected by co-culture with plasma isolated from mice fed a high fat (HF) diet (Figures 3B, S3D) (27) that had fatty livers without any discernible changes in their hepatic metal ion content or the abundance of core subunits of each OXPHOS enzyme complex (Figure S3B, C). In contrast, boiling or trypsin treatment of *Sco1*^{hep} plasma abolished its negative effect on PBMC viability (Figure 3C),

suggesting that the secreted factor is a protein. We therefore fractionated plasma proteins based on size and the presence of a glycan, and found that the bioactivity was retained in a >50 kDa glycoprotein-containing fraction (Figure 3C).

To identify the secreted factor, the >50kDa glycoprotein-containing *Control*, *hep* and *HF* plasma fractions were analyzed by quantitative mass spectrometry (MS) (Figure 4A). We reasoned that the immunosuppressive factor would be absent in *HF* plasma, enriched in *hep* plasma and more abundant in $Sco1^{hep}$ than $Cox10^{hep}$ plasma, given the relative severity of the leukopenia in each model. Of the two up-regulated hits, only AFP met those criteria (Figures 4A, S4A). Consistent with our MS results, AFP abundance was elevated in P47 $Sco1^{hep}$, P77 $Coa5^{hep}$ and P64 $Cox10^{hep}$ plasma (Figure 4B), and its circulating levels were significantly higher in $Sco1^{hep}$ than *Control* plasma at P27 and continued to increase as the severity of the leukopenia worsened over time (Figure 4C). In fact, the roughly 2000-fold difference in AFP abundance between *Control* and $Sco1^{hep}$ plasma in P47 mice was mirrored at the transcript level in the $Sco1^{hep}$ liver (Figure S4B), emphasizing that the liver is the principal organ responsible for secreting AFP into the circulation.

To further validate AFP as the active component of our signaling axis, we investigated the effect of manipulating its abundance on WBC viability both *in vitro* and *in vivo*. The viability of PBMCs co-cultured in $Sco1^{hep}$ plasma was rescued upon immunodepletion of AFP but not by pre-treatment of plasma with anti-SLC25A3, an isotype antibody control (Figure 4D). Supplementation of standard media with recombinant AFP (rAFP) alone also induced PBMC death (Figure S4C). Corroborating our *in vitro* findings, serial injection of 21-24 day old *Control* mice with rAFP, but not with the closely related family member albumin, resulted in a leukopenia of comparable severity to that seen in *Control* mice injected with $Sco1^{hep}$ plasma

(Figure 4E). These data collectively argue that AFP secreted by the liver is directly responsible for the unexpected immunosuppression we observe in our *hep* mouse models of mitochondrial disease.

AFP can be produced by non-hepatic models of mitochondrial dysfunction and requires copper for its immunosuppressive activity

AFP is highly expressed during embryonic development and is also secreted by the yolk sac, stomach and cells of the intestine (28). While its expression is repressed post-birth by epigenetic mechanisms (29, 30), it is known that the adult liver re-activates the *AFP* locus and secretes the protein in response to fibrosis, hepatitis and several hepatic cancers (31-33). We therefore investigated whether mitochondrial dysfunction is a general trigger for AFP overexpression in other cell types. To test this idea, we treated the murine myoblast C2C12 cell line with pharmacological agents to inhibit specific OXPHOS complexes. Indeed, specific inhibition of COX (Complex IV) and Complexes I, III or V resulted in a modest but significant increase in steady-state AFP levels (Figure 4F, G). To determine whether this is a cell-type dependent phenotype, we treated two additional cell types with Complex IV inhibitor and found that skeletal myoblasts and B-lymphocytes, but not fibroblasts, up-regulated AFP production in response to COX inhibition (Figure 4H, I). These data suggest that in addition to hepatocytes, several other cell types are able to increase AFP production in response to mitochondrial dysfunction. To expand upon our pharmacological analyses, we investigated whether AFP expression is upregulated in the muscle of a whole animal model with secondary mitochondrial dysfunction. We found that COX-deficient murine hearts lacking the high affinity copper importer CTR1 (34) indeed have significantly higher levels of *Afp* transcript (Figure S5A) and

protein (Figure S5B), along with elevated levels of the ISR marker phospho-eIF2α (Figure S5B) when compared to the hearts of *Control* littermates. Taken together, these findings indicate that mitochondrial dysfunction triggers re-activation of AFP expression in diverse cell types and tissues.

Several proteoforms of AFP are known to be present in the general circulation and at least some of these have the ability to bind a variety of ligands, including copper (35). Therefore, an intriguing possibility is that the leukopenia in *hep* mice is caused by a specific conformer(s) constituting a fraction of the total plasma AFP pool. To address this possibility, we took further advantage of the $Ctr1^{hrt}$ mouse model because its COX-deficient heart is known to communicate with the liver leading to a significant hepatic copper deficiency (34). Like several of our *hep* models, P10 $Ctr1^{hrt}$ mice exhibited disproportionate atrophy of the spleen and thymus (Figure 5A) and a significant leukopenia (Figure 5B). Due to their young age, circulating AFP levels were comparable in *Control* and $Ctr1^{hrt}$ animals (Figure 5C); however, only $Ctr1^{hrt}$ plasma was capable of killing PBMCs (Figure 5D). This observation is consistent with the idea that AFP abundance alone does not explain its immunosuppressive properties. In fact, $Ctr1^{hrt}$ and $Sco1^{hep}$ plasma pre-treated with the Cu(I)-specific chelator bathocuproine disulfonic acid (BCS) prevented PBMC death (Figure 5D, E) whereas the addition of copper salts to the culture media enabled the AFP-rich, age-matched (P10) *Control* plasma to stimulate PBMC death (Figure 5D). Consistent with these observations, PBMC viability was unaffected upon co-culture with recombinant AFP produced and isolated from *E. coli* (Figure S5C), where free copper is known to be very scarce in the cytosol (36). Collectively, these data argue that AFP requires copper to induce cell death in WBCs and cause a leukopenia.

AFP promotes the death of mouse and human PBMCs via the CCR5 receptor

To establish that AFP causes a leukopenia by stimulating WBC death, we isolated PBMCs from P47 *Control* and *Sco1*^{hep} mice and cells positive for CD44, a marker of activation, and annexin V, an indicator of cell death. Both markers were significantly elevated in *Sco1*^{hep} PBMCs when compared to *Control* PBMCs (Figures 6A, S6), consistent with the idea that AFP indeed stimulates WBC death. To confirm our *in vivo* observations and further delineate the temporal relationship between activation and cell death in the presence of bioactive AFP, we conducted a time course experiment using naïve, wild-type PBMCs co-cultured in *Control* or *Sco1*^{hep} plasma. At 12 hours, CD44 staining was significantly higher in PBMCs grown in media containing *Sco1*^{hep} plasma while annexin V staining was similar in *Control* and *Sco1*^{hep} co-cultures (Figure 6B, C). Annexin V positive cell numbers then increased significantly in the *Sco1*^{hep} co-culture over the next 36 hours (Figure 6B), indicating that activated PBMCs were indeed dying.

It has been proposed that AFP exerts its immunosuppressive effects by binding to various cation channels and classes of receptors that include mucin, scavenger, lysophospholipid and chemokine receptors (37-42). To date, however, AFP has only been shown to bind directly to the chemokine receptor CCR5 (43). We therefore co-cultured PBMCs in *Control* or *Sco1*^{hep} plasma alone or in media that also contained the CCR5 antagonist Maraviroc (44) and found that receptor blocking rescued cell viability (Figure 6D). To determine if AFP from our *hep* mouse models of mitochondrial disease also acts in an immunosuppressive manner on human cells via the same mechanism, we repeated the experiment and found that pharmacologically blocking the CCR5 receptor ablated the ability of *Sco1*^{hep} plasma to kill human PBMCs (Figure 6D). Taken together, our data argue that AFP requires both copper and CCR5 to activate and kill WBCs to

induce a leukopenia. Our findings further establish that this immunosuppressive mechanism is also capable of triggering the death of human PBMCs and suggest that tissue release of a specific AFP conformer in response to mitochondrial dysfunction provides a mechanism to suppress the peripheral immune system.

Discussion

Here, we uncover a molecular mechanism by which a primary mitochondrial dysfunction in the liver compromises the peripheral immune system, revealing the basis of a surprising inter-tissue signaling circuit. We demonstrate that a defect in OXPHOS in the post-natal mouse liver induces robust secretion of AFP which, in concert with copper, activates cell death in leukocytes by interacting with the cell surface receptor CCR5. In turn, this leads to a progressive leukopenia and atrophy of the thymus and spleen. Patients with inherited mitochondrial disorders are well-known to be susceptible to acute febrile infections (45) and in some cases manifest with congenital neutropenia (46); however, a molecular basis for these phenotypes has been lacking until now. Together, our findings identify an immunosuppressive mechanism that could account for why some groups of patients with mitochondrial dysfunction are vulnerable to infections. It may also explain why patients with elevated circulating AFP levels owing to ataxia telangiectasia or other cerebellar ataxias with suspected mitochondrial involvement are also prone to recurrent infection (47, 48). However, considering the tremendous clinical heterogeneity of mitochondrial diseases it is likely that additional mechanisms contribute to immunosuppression in a context-dependent manner that have yet to be identified.

AFP is a major serum protein expressed by the developing embryo that is under tight temporal and spatial regulation (29, 49). Post-birth, multiple genetic factors coordinate a

conserved developmental program to repress transcription via elements upstream of the gene promoter (30, 50, 51). However, liver dysfunction in adults can reactivate AFP expression in hepatocytes, most notably with hepatic cellular carcinoma (HCC) and fibrosis (31, 33). Though the precise functional consequence of AFP secretion in these disease settings is poorly understood, it has been suggested to increase hepatocyte cell proliferation in HCC. In the context of mitochondrial dysfunction, hyperplasia of hepatocytes is not observed (18) nor are high circulating levels of AFP alone toxic to leukocytes. Instead, the leukocyte toxicity requires AFP and copper, a known ligand of this serum protein (35).

Copper is an essential metal that acts as a co-factor for select cellular enzymes catalyzing redox reactions. This trace element is obtained from the diet and then systemically distributed to meet cellular demand. In mammals, the liver acts as the principal storage tissue to coordinate systemic copper levels, a function that is of utmost importance in early post-natal life and in response to copper handling defects in other tissues. Intracellular copper is trafficked by a series of dedicated chaperones that form an effective delivery pathway to target enzymes for metalation or labile pools for storage (52). Many of the central factors for copper transport have been elucidated and disruptions to these steps can exert devastating effects on human health. In our mouse models of mitochondrial dysfunction, we observe a signature of disrupted copper homeostasis in the liver and a responsive cascade of subsequent compensatory events. This response initiates with the progressive loss of the CTR1 copper transporter in the liver via proteasomal degradation, effectively reducing copper uptake (18). However, a shift to enhance copper efflux from the tissue likely follows, given that the levels of copper and the copper-dependent ferroxidase ceruloplasmin are both elevated in *hep* plasma (18). Consistent with an important role for hepatic copper mobilization in the observed immune phenotypes, the liver of

Ctr1^{hrt} mice upregulates ATP7A expression and pumps copper into the circulation as a consequence of loss of CTR1 function in the heart, a response that renders it copper-deficient relative to the liver of wild-type littermates (34).

To reconcile our findings, we propose the following model. The induction of AFP synthesis in response to mitochondrial dysfunction coincides with the cellular response to increased copper efflux into the secretory system. Although the exact role of copper in potentiating the immunosuppressive properties of AFP is currently unclear, we speculate that for AFP to be cytotoxic to leukocytes it chelates copper during secretion from hepatocytes. Central to this model is the role of mitochondria in regulating liver copper homeostasis (18, 53-55). We hypothesize that the coupling of these two molecular events is required for the observed leukopenia.

Our model accounts for the apparent inert activity of high circulating levels of AFP in the early post-natal period and the absence of a leukopenia with HCC. Further, the model makes clear predictions that disruptions to copper efflux into the secretory system would ablate the AFP driven leukocyte toxicity. Copper delivery to the secretory system is mediated via ATOX1 to the ATPase copper pumps, ATP7A and ATP7B (56). Pathogenic variants in *ATP7A* and *ATP7B* manifest as Menkes and Wilson disease, respectively (57, 58). In line with our model, neither disorder is characterized by immune suppression or neutropenia, even though severe liver pathology is a hallmark of Wilson disease (59). Mitochondrial signaling has previously been shown to promote cellular copper efflux (54, 55), and the most severe leukopenias in our *hep* models coincide with higher levels of copper in the circulation. While these findings support the notion that sufficient ATP7A and ATP7B remains localized within the secretory system to account for the observed phenotypes in liver experiencing mitochondrial dysfunction, future

investigations will be required to untangle the trafficking dynamics of the efflux transporters in hepatocytes under these conditions.

A key question remains, which is how is the transcriptional suppression of AFP expression released? Although we observe ISR activation upon mitochondrial dysfunction in the liver, it may be that it is not the signaling cascade that regulates AFP induction. ISR activation is emerging as a robust stress response to mitochondrial OXPHOS dysfunction in patients and in animal models of these diseases (10, 11, 60-62). The signaling cascade leads to the induction and secretion of two growth factors, GDF15 and FGF21, that remodel cellular metabolism in response to nutritional and metabolic disturbances. Thus, while induction of this stress response is not surprising in our mouse models, ISR activation in other mitochondrial disorders caused by OXPHOS dysfunction is not always accompanied by increased AFP expression or a leukopenia (63, 64). This suggests a cell-type specific mechanism whereby severe disruptions to hepatocyte homeostasis overide the transcriptional repression of AFP. We propose instead that the central role of mitochondrial signaling in regulating copper homeostasis in the liver likely underpins the mechanism for AFP immunosuppression. The basis of this pathway opens up an exciting new avenue for the role of mitochondria in intracellular signaling.

Another outcome of our study is the identification of a potential new biomarker of mitochondrial dysfunction in the liver. Currently, GDF15 and FSF21 are robust biomarkers detected in the circulation of patients with specific classes of mitochondrial disorders, particularly with skeletal muscle involvement (11, 61, 62, 65, 66). Interestingly, these biomarkers were first identified in mouse models of mitochondrial myopathy, including those with a *Cox10* deficiency (67). This highlights the promise of translating discoveries derived from mouse models of mitochondrial disorders into robust clinical practice for non-invasive patient

diagnostics. Future studies with large cohorts of patients screened for circulating AFP expression and bioactivitywill need to be performed as previous experience emphasizes that not all mitochondrial diseases induce GDF15 and FGF21 expression (11), further arguing that there is specificity in the systemic response to mitochondrial dysfunction.

In conclusion, we identify a novel tissue crosstalk mechanism whereby the homeostatic role of mitochondria in coordinating hepatic copper homeostasis intersects with the function of the peripheral immune system. Diet could also be a key factor in modulating the response, particularly with foods rich in copper. Future studies will explore the role of this leukopenia mechanism in the underlying susceptibility of patients with mitochondrial disease or ataxia telangiectasia to infections.

Materials and Methods

Animal models and husbandry

Homozygous floxed *Sco1*, *Cox10* and *Coa5* mice were used to generate hepatocyte-specific (*hep*) knockout models as previously described (18). Briefly, floxed animals were crossed with mice in which *Cre* recombinase expression is driven by the albumin promoter (*Alb-Cre*$^{tg/tg}$). *Cre* positive, F1 progeny were then backcrossed to the appropriate homozygous floxed model to generate F2 litters, with roughly 25% of the resultant progeny exhibiting hepatocyte-specific loss of expression of the gene of interest.

Heart-specific *Ctr1* (*Ctr1*^{hrt}) knockout mice were generated according to (34). PCR genotyping of *Sco1* (18), *Cox10* (22) and *Ctr1* (34) mice was as previously described, and age-matched *flox/+* or *flox/flox* siblings served as *Controls* in this study. *Coa5* mice were genotyped as detailed below. Mice were housed under a 12hr light: 12hr dark photoperiod in a temperature and humidity-controlled facility and provided with food and water *ad libitum*.

Generation of a conditional Coa5 mouse model

ES cells with floxed *Coa5* alleles were purchased from the Knockout Mouse Project (KOMP) Repository. Male chimera transmitter *Coa5* mice lacking the neomycin-resistance cassette and *lacZ* reporter gene were then generated fee-for-service at the Toronto Centre for Phenogenomics and shipped to the University of Saskatchewan. These males were crossed with C57BL/6N females, and the resultant $Coa5^{loxP/wt}$ progeny were intercrossed to yield homozygous *Coa5* mice with a residual FRT site and loxP sites that flank the second exon of the gene to allow for its deletion.

Specimen collection

Mice were weighed prior to being anesthetized with 2% isofluorane. Blood was then collected from the left ventricle of the heart using a 27-gauge needle, placed into a precoated K_2EDTA tube, and inverted 10 times. After a 20 minute room temperature incubation, 100ml of blood was retained on ice for further analyses while the remainder was used to isolate plasma by two sequential room temperature spins for 5 minutes at 1,000 *x g*.

Following blood collection, the thymus, heart, spleen, liver, kidney and brain were harvested, and flash frozen on dry ice in pre-weighed Eppendorf tubes. Tubes were then weighed post-collection, allowing for tissue wet weights to be calculated. Tissues were then powdered in a stainless-steel mortar and pestle on dry ice and stored at -80^{o}C for subsequent biochemistry, molecular biology, elemental and genetic analyses.

Complete blood cell count (CBC) and peripheral blood smear

Automated CBC analysis was performed on the fraction of retained blood using the COULTER® Ac·T diff™ Analyzer (Beckman). All samples were run in duplicate. Alternatively, a spreader slide and 10µl of blood were used to create a peripheral blood smear. Air-dried slides were then stained with Wright's Geimsa using an immersion protocol. Briefly, slides were stained for 1 minute, rinsed for 5 min in phosphate buffer (pH 6.8) (made with potassium phosphate, monobasic 50.1% (w/w) and sodium phosphate, dibasic 49.9% (w/w)), washed briefly in running deionized water, dried and cover slipped. The white blood cell (WBC) count was determined by taking the average number of WBCs in 10 fields at 40X high power and multiplying by $2.0x10^9$/L (*66*).

Tissue perfusion, fixation and histology

Mice were anesthetized with 2-3% isoflurane and oxygen, and perfused through the heart with 10 ml HBSS (pH 7.2) containing 2.5% FBS at a flow rate of ~5ml/min. Once the organs were cleared of blood, mice were perfused with another 10 ml of 10% formalin. The thymus, heart, spleen and liver were harvested, stored overnight in 10% formalin, then dehydrated and embedded in paraffin. Seven micrometer cross-sections were prepared, and slides were stained with hematoxylin and eosin (H&E) according to the manufacturer's standard procedure. Sections were viewed and imaged using a scanning transmission light microscope (Leica).

Adenoviral-related experiments

Helper-dependent adenovirus (HdAD) encoding the *lacZ* transgene or vehicle (sterile Ringer's solution) were administered via intracardiac (IC) or interperitoneal (IP) injection. We found that IC administration resulted in higher β-galactosidase expression in the liver with less intense

staining in other, peripheral tissues when compared to IP injection (Fig. S1B). We therefore used the IC route to administer $5.783x10^{12}$ *Sco1* HdAD particles/kg or an equivalent volume of vehicle to mice at 21-24 days of age. Mice were anesthetized with 2% isofluorane, the chest and abdomen were disinfected with 70% ethanol, and adenovirus or vehicle was administered with a 27-gauge needle by direct puncture of the left ventricle through the diaphragm following the drawback of fresh arterial blood. Blood and tissues were then collected when mice reached 47 days of age.

Immunoblot analyses

Powdered whole tissues were resuspended and homogenized on ice in extraction buffer (68) supplemented with a complete protease inhibitor cocktail (Roche) and 0.5mM PMSF. Following a 30 min incubation step on ice, lysates were clarified by centrifugation at 16,600 *x g* for 10 minutes at 4^{o}C and equal amounts of protein (10-25μg/lane) were electrophoresed on 4-20% pre-cast Tris-HCl gels (BioRad). All gels were then transferred onto nitrocellulose membrane under semi-dry conditions and blotted with the appropriate antibodies. Following incubation of membranes with secondary antibody, immunoreactive proteins were detected by luminol enhanced chemiluminescence. For cultured cells, 2 X 10^5 cells were seeded on a 6 well plate and treated with either DMSO or OXPHOS inhibitors including Rotenone (1 μM), Malonate (1 mM), Antimycin (1 μM), KCN (1 mM), Oligomycin (1 μM) for 24 hours. Cells were washed with PBS and harvested using a cell scraper. Cells were then lysed in RIPA buffer supplemented with protease inhibitor cocktail (Roche). After 30 min incubation in lysis buffer, cell lysates were collected by centrifugation at 14, 000 *x g* for 10 mins at 4˚C and equal amounts of protein (20 μg) were electrophoresed on 10% pre-cast Bis-Tris gels (Life Technologies). Following semi-dry

transfer of gels onto PVDF membranes, the membranes were blotted with indicated antibodies (anti-AFP obtained from Leary Lab and anti-β-actin from Sigma A2228) and protein bands detected as above.

Elemental analyses

Samples were digested in 40% nitric acid by boiling for 1 hour in capped, acid washed tubes, diluted in ultra pure, metal free water and analyzed by ICP-OES (Perkin Elmer, Optima 7300DV) versus acid washed blanks. Concentrations were determined from a standard curve constructed with serial dilutions of two commercially available mixed metal standards (Optima). Blanks of nitric acid with and without "metal-spikes" were analyzed to ensure reproducibility.

qPCR analyses

Total RNA was extracted with Trizol Reagent and quantified using a Nanodrop. cDNA was synthesized using Superscript IV Reverse Transcriptase and Oligo(dT)20 primers from ThermoFisher. qPCR was performed using SsoFast EvaGreen Supermix (Bio-Rad) on a CFX384 Touch Real-Time PCR Detection System (Bio-Rad). Data were analyzed according to the delta delta Ct method and *Afp* levels were normalized against *Gadph* abundance.

ATP quantitation

ATP levels in $Sco1^{hep}$, $Cox10^{hep}$, $Coa5^{hep}$ and age-matched littermate *Control* livers were measured using a luminescent detection kit, as per the manufacturer's instructions. Briefly, 10mg of powdered liver tissue was homogenized in 2.5% trichloroacetic acid (TCA), sonicated on ice and neutralized with Tris-acetate buffer. Signal intensities were read using a Luminex multimode

plate reader. Arbitrary luminescence units in *hep* livers were represented as the fold change relative to the appropriate *Control* group.

Tail vein injections

Plasma for tail vein injections was aseptically pooled, aliquoted and stored at -80^{o}C prior to the beginning of an experiment. *Control* mice were injected via the tail vein between 24 and 27 days of age with a 27-gauge needle, after tails had been warmed for 5-10 min under a heat lamp and subsequently cleaned with 70% ethanol to prevent infection. Animals were injected with the maximum recommended volume of 10ml/kg or 100-200µl of plasma isolated from *Control* or *Sco1*^{hep} mice, or with 1µg of rAFP or albumin, a closely related family member. Mice were injected every 72 hours thereafter for a 28 day period. Blood and tissues were collected 3 days after the eighth injection.

PBMC isolation and culture

Mouse blood was collected as described above. Human blood was obtained from three consenting, healthy volunteers (30-50 years of age) and used in experiments approved by the Research Ethics Board at the University of Saskatchewan. Both mouse and human PBMCs were isolated by Ficoll Plaque Plus density centrifugation, and cultured at a concentration of 10^6 cells/ml in RPMI 1640 media supplemented with 20% FBS and 100 IU IL-2. All related experiments were carried out one to three days after PBMCs were initially isolated.

PBMC viability assays were quantified by counting the number of live and dead/dying cells in bright-field photomicrographs acquired at 60x magnification. Cell counting was performed by an observer who was blind to the treatment conditions, using the Point Tool in

ImageJ (https://imagej.nih.gov/ij/). Cells were defined as alive or dead/dying based on their size and morphology. Round cells with a diameter ≥ 5 µm and with an intact cell membrane were defined as live cells. Round cells with a diameter of ≤ 3 µm, and cells with a diameter≥ 3 µm that exhibit obvious signs of cell blebbing (a hallmark of apoptosis), were defined as dead/dying cells. For each photomicrograph, the % dead cells was calculated as [number of dead or dying cells]/[number of dead or dying cells + number of live cells] x 100%. Three to 13 images were quantified per treatment condition, acquired from 5 independent experiments.

Plasma fractionation and PBMC treatment

Plasma pools were generated for *Sco1*^{hep}, *Cox10*^{hep} and age-matched littermate *Control* animals. Plasma from mice fed a high fat (HF) diet (27) was also obtained, pooled and used as an additional control. PBMCs were cultured as described above in media containing 20% FBS or 17.5% FBS and 2.5% *Control*, *hep* or *HF* plasma.

To determine if the bioactive factor in *hep* plasma was a protein and the nature of that protein, plasma from *Control* and *Sco1*^{hep} mice was first boiled for 5 min at 98°C or treated with trypsin for 1 hr. PBMCs were then cultured as described above in media containing 17.5% FBS plus 2.5% untreated, boiled or trypsinized plasma from *Control* or *Sco1*^{hep} mice. Control and *hep* plasma was then separated by size using centrifugal 50KDa Filters (Amicon) and by glycan content using the Qproteome Total Glycoprotein Kit, with both steps being done according to the manufacturer's instructions. PBMCs were cultured as described above in media supplemented with 17.5% FBS containing 2.5% of each plasma fraction.

For AFP depletion experiments, a volume of plasma equivalent to 2.5% v/v from *Control* or *Sco1*^{hep} mice was incubated with 1µg mouse anti-AFP and rotated at 4°C overnight. 250µl of

protein A dynabeads was then added to the plasma and incubated at room temperature for 2 hours. Mouse anti-SLC25A3 was used as an IgG isotype control. Antibody-bead complexes were collected on a magnet, and the resultant plasma was used to treat PBMCs as described above. *Control* and *Sco1*^{hep} plasma that had been incubated with an equivalent volume of PBS served as internal controls.

Mass Spectroscopy (MS) and differential analysis

Quantitative MS analyses were conducted fee-for-service by the Proteomics platform at the McGill University Health Centre. Briefly, 2µg of the >50kDa glycosylated plasma fraction from *Control*, *Sco1*^{hep}, *Cox10*^{hep} and *HF* mice was trypsinized and analyzed using a Thermo Scientific Ultimate 3000 HPLC and Orbitrap Fusion MS: Quadrupole-Orbitrap-Linear ion trap hybrid. Raw data was then mined with Pinnacle (http://www.optystech.com/index.html#) and the spectral counts for each peptide were quantified. Only proteins for which two unique peptides were detected were included in the final analyses, and quantitative data for each experimental group represent the average of two independent MS runs.

Liquid chromatography MS (LCMS) differential analysis was performed using R (*67*). The package DESEQ2 (*68*) was used to test for differential expression, the package data.table (*69*) was used for data manipulation and ggplot2 was used to generate plots (*70*). Raw data was imported (20190508_LCMS_raw_data_sheet1) and counts were converted to integers. Counts with NA were converted to zero. One count was added to all samples. The count matrix was prepared (20190508_input_sheet2) and DESeq2 was performed on *hep* vs *Control*. A false discovery rate (FDR) of 0.1 was applied to report significant (upregulated/downregulated) versus non-significant (ns) hits (20190508_results_sheet3).

Flow Cytometry

PBMCs isolated from *Control* and *Sco1*^{hep} blood was stained with an anti-CD45, CD3, CD4, CD25, CD44 and CD69 antibody cocktail or with an anti-CD3, CD4, 7AAD and Annexin V antibody mixture. Briefly, PBMCs were resuspended in PBS with 2.5% FBS at 1×10^6 cells/mL. Cells were blocked with anti-mouse CD16/CD32 Fc block for 15 min and then incubated with the primary antibody cocktail for 30 min. For cells stained with Annexin V, PBMCs were resuspended and blocked as described above, and then incubated with anti-CD3 and anti-CD4 for 20 min. 7AAD antibody was subsequently added to the staining mixture and further incubated for 10 min. Cells were then centrifuged for 5 min at 1000 *x g*, resuspended in Annexin V binding buffer and stained according to the manufacturer's instructions. Following either staining procedure, cells were fixed in a solution of 1% formalin with red cell lysing solution for 15 min. All events were analyzed using a CellFlex™ Flow Cytometer (Beckman Coutler). Dead cells were excluded based on forward and side light scattering. All antibody staining procedures took place at room temperature in the dark.

Quantification and statistical analysis

All statistical analysis was performed using GraphPad Prism 8.0 or 9.0. Data were reported as mean ± SEM. For selection of appropriate statistical tests, data were assessed by histogram or Tukey plot to detect a normal Gaussian distribution. After verifying a Gaussian distribution, statistical differences between two groups were assessed using a Student's t-test and between three or more groups with a one-way ANOVA and a Tukey's or Sidak post-hoc test. For the qPCR analyses in Figure S5, differences in *Afp* mRNA abundance between the *Control* and

Ctr1^{hrt} hearts were assessed using a non-parametric Mann-Whitney U test as the data were not normally distributed. For data with two independent variables, a two-way ANOVA and Bonferonni's post-hoc test was used. p-values <0.05 were considered significant. Statistical parameters can be found in the figure legends.

Study approval

All experiments on F2 *hep* animal models were approved by the Animal Ethics Review Board at the University of Saskatchewan (AUP# 20100091, S.C.L.) while those involving the *Ctr1* mouse model were conducted in accordance with National Institutes of Health Guide and approved by the Institutional Animal Care and Use Committee at the University of Maryland, College Park (AUP# R-APR-18-14, B.-E.K).

Author contributions

SCL and KAJ conceived the original study, while KAJ, PAC, B-EK, H-YMC, VMG and SCL contributed to its further refinement. Data were collected by KAJ, ZNB, AB, MAH, OY, PAC, SG, KB, SY and CL, and analyzed by KAJ, SG, KB, CL, OHMHA and SY. JD, PN, KM, CS and GNI provided guidance, reagents or samples invaluable to experimental advancement. The manuscript was written by SCL, BJB and KAJ and edited by PAC, BJB, B-EK, H-YMC and VMG.

Acknowledgements

The authors are indebted to Drs. Dennis J. Thiele (Sisu Pharma), Eric A. Shoubridge (McGill University), Dennis Winge (Utah University), Kerry Lavender and Scott Wiedenmaier

(University of Saskatchewan) for helpful discussions. Funding: This work was supported by grants-in-aid of research from the Canadian Institutes for Health Research (MOP16652, S.C.L.), National Institutes of Health (DK110195, B.-E.K.; GM120211, P.A.C and S.C.L; GM111672, V.M.G), and an X-grant from Texas A&M University (V.M.G). PAC is supported by the Alabama Agricultural Experiment Station. Competing interests: The authors do not have any competing interests, financial or otherwise.

References

1. Rajan A, and Perrimon N. Drosophila as a model for interorgan communication: lessons from studies on energy homeostasis. *Dev Cell.* 2011;21(1):29-31.
2. Taylor RC, Berendzen KM, and Dillin A. Systemic stress signalling: understanding the cell non-autonomous control of proteostasis. *Nat Rev Mol Cell Biol.* 2014;15(3):211-7.
3. Deng P, and Haynes CM. The mitokine quest(ion). *Cell Res.* 2016;26(12):1265-6.
4. Schinzel R, and Dillin A. Endocrine aspects of organelle stress-cell non-autonomous signaling of mitochondria and the ER. *Curr Opin Cell Biol.* 2015;33:102-10.
5. Droujinine IA, and Perrimon N. Interorgan Communication Pathways in Physiology: Focus on Drosophila. *Annu Rev Genet.* 2016;50:539-70.
6. Suomalainen A, and Battersby BJ. Mitochondrial diseases: the contribution of organelle stress responses to pathology. *Nat Rev Mol Cell Biol.* 2018;19(2):77-92.
7. Pakos-Zebrucka K, Koryga I, Mnich K, Ljujic M, Samali A, and Gorman AM. The integrated stress response. *EMBO Rep.* 2016;17(10):1374-95.
8. Fessler E, Eckl EM, Schmitt S, Mancilla IA, Meyer-Bender MF, Hanf M, et al. A pathway coordinated by DELE1 relays mitochondrial stress to the cytosol. *Nature.* 2020;579(7799):433-7.
9. Guo X, Aviles G, Liu Y, Tian R, Unger BA, Lin YT, et al. Mitochondrial stress is relayed to the cytosol by an OMA1-DELE1-HRI pathway. *Nature.* 2020;579(7799):427-32.
10. Mick E, Titov DV, Skinner OS, Sharma R, Jourdain AA, and Mootha VK. Distinct mitochondrial defects trigger the integrated stress response depending on the metabolic state of the cell. *Elife.* 2020;9.
11. Lehtonen JM, Forsstrom S, Bottani E, Viscomi C, Baris OR, Isoniemi H, et al. FGF21 is a biomarker for mitochondrial translation and mtDNA maintenance disorders. *Neurology.* 2016;87(22):2290-9.
12. DiMauro S, and Schon EA. Mitochondrial respiratory-chain diseases. *N Engl J Med.* 2003;348(26):2656-68.
13. Parikh S, Goldstein A, Karaa A, Koenig MK, Anselm I, Brunel-Guitton C, et al. Patient care standards for primary mitochondrial disease: a consensus statement from the Mitochondrial Medicine Society. *Genet Med.* 2017;19(12).
14. West AP, Shadel GS, and Ghosh S. Mitochondria in innate immune responses. *Nat Rev Immunol.* 2011;11(6):389-402.

15. Clarke SL, Bowron A, Gonzalez IL, Groves SJ, Newbury-Ecob R, Clayton N, et al. Barth syndrome. *Orphanet J Rare Dis.* 2013;8:23.
16. Manea EM, Leverger G, Bellmann F, Stanescu PA, Mircea A, Lebre AS, et al. Pearson syndrome in the neonatal period: two case reports and review of the literature. *J Pediatr Hematol Oncol.* 2009;31(12):947-51.
17. Walker MA, Slate N, Alejos A, Volpi S, Iyengar RS, Sweetser D, et al. Predisposition to infection and SIRS in mitochondrial disorders: 8 years' experience in an academic center. *J Allergy Clin Immunol Pract.* 2014;2(4):465-8, 8 e1.
18. Hlynialuk CJ, Ling B, Baker ZN, Cobine PA, Yu LD, Boulet A, et al. The Mitochondrial Metallochaperone SCO1 Is Required to Sustain Expression of the High-Affinity Copper Transporter CTR1 and Preserve Copper Homeostasis. *Cell Rep.* 2015;10(6):933-43.
19. Postic C, and Magnuson MA. DNA excision in liver by an albumin-Cre transgene occurs progressively with age. *Genesis.* 2000;26(2):149-50.
20. Brunetti-Pierri N, and Ng P. Helper-dependent adenoviral vectors for liver-directed gene therapy. *Hum Mol Genet.* 2011;20(R1):R7-13.
21. Brunetti-Pierri N, Ng T, Iannitti D, Cioffi W, Stapleton G, Law M, et al. Transgene expression up to 7 years in nonhuman primates following hepatic transduction with helper-dependent adenoviral vectors. *Hum Gene Ther.* 2013;24(8):761-5.
22. Diaz F, Garcia S, Hernandez D, Regev A, Rebelo A, Oca-Cossio J, et al. Pathophysiology and fate of hepatocytes in a mouse model of mitochondrial hepatopathies. *Gut.* 2008;57(2):232-42.
23. Harding HP, Zhang Y, Zeng H, Novoa I, Lu PD, Calfon M, et al. An integrated stress response regulates amino acid metabolism and resistance to oxidative stress. *Mol Cell.* 2003;11(3):619-33.
24. Pathak VK, Schindler D, and Hershey JW. Generation of a mutant form of protein synthesis initiation factor eIF-2 lacking the site of phosphorylation by eIF-2 kinases. *Mol Cell Biol.* 1988;8(2):993-5.
25. Krysko DV, Agostinis P, Krysko O, Garg AD, Bachert C, Lambrecht BN, et al. Emerging role of damage-associated molecular patterns derived from mitochondria in inflammation. *Trends Immunol.* 2011;32(4):157-64.
26. Kim SJ, Xiao J, Wan J, Cohen P, and Yen K. Mitochondrially derived peptides as novel regulators of metabolism. *J Physiol.* 2017;595(21):6613-21.
27. Savard C, Tartaglione EV, Kuver R, Haigh WG, Farrell GC, Subramanian S, et al. Synergistic interaction of dietary cholesterol and dietary fat in inducing experimental steatohepatitis. *Hepatology.* 2013;57(1):81-92.
28. Jones EA, Clement-Jones M, James OF, and Wilson DI. Differences between human and mouse alpha-fetoprotein expression during early development. *J Anat.* 2001;198(Pt 5):555-9.
29. Belayew A, and Tilghman SM. Genetic analysis of alpha-fetoprotein synthesis in mice. *Mol Cell Biol.* 1982;2(11):1427-35.
30. Vacher J, and Tilghman SM. Dominant negative regulation of the mouse alpha-fetoprotein gene in adult liver. *Science.* 1990;250(4988):1732-5.
31. Abelev GI. Alpha-fetoprotein in ontogenesis and its association with malignant tumors. *Adv Cancer Res.* 1971;14:295-358.
32. Castaneda JA, and Pearce DA. Identification of alpha-fetoprotein as an autoantigen in juvenile Batten disease. *Neurobiol Dis.* 2008;29(1):92-102.

33. Nakano Y, Nakao S, Sumiyoshi H, Mikami K, Tanno Y, Sueoka M, et al. Identification of a novel alpha-fetoprotein-expressing cell population induced by the Jagged1/Notch2 signal in murine fibrotic liver. *Hepatol Commun.* 2017;1(3):215-29.
34. Kim BE, Turski ML, Nose Y, Casad M, Rockman HA, and Thiele DJ. Cardiac copper deficiency activates a systemic signaling mechanism that communicates with the copper acquisition and storage organs. *Cell Metab.* 2010;11(5):353-63.
35. Aoyagi Y, Ikenaka T, and Ichida F. Copper(II)-binding ability of human alpha-fetoprotein. *Cancer Res.* 1978;38(10):3483-6.
36. Arguello JM, Raimunda D, and Padilla-Benavides T. Mechanisms of copper homeostasis in bacteria. *Front Cell Infect Microbiol.* 2013;3:73.
37. Zhu W, Peng Y, Wang L, Hong Y, Jiang X, Li Q, et al. Identification of alpha-fetoprotein-specific T-cell receptors for hepatocellular carcinoma immunotherapy. *Hepatology.* 2018;68(2):574-89.
38. Newby D, Dalgliesh G, Lyall F, and Aitken DA. Alphafetoprotein and alphafetoprotein receptor expression in the normal human placenta at term. *Placenta.* 2005;26(2-3):190-200.
39. Mizejewski GJ. Review of the Third Domain Receptor Binding Fragment of Alphafetoprotein (AFP): Plausible Binding of AFP to Lysophospholipid Receptor Targets. *Curr Drug Targets.* 2017;18(7):874-86.
40. Mizejewski GJ. The alpha-fetoprotein third domain receptor binding fragment: in search of scavenger and associated receptor targets. *J Drug Target.* 2015;23(6):538-51.
41. Mizejewski GJ. The adenocarcinoma cell surface mucin receptor for alpha-fetoprotein: is the same receptor present on circulating monocytes and macrophages? A commentary. *Tumour Biol.* 2014;35(8):7397-402.
42. Mizejewski GJ. Review of the putative cell-surface receptors for alpha-fetoprotein: identification of a candidate receptor protein family. *Tumour Biol.* 2011;32(2):241-58.
43. Atemezem A, Mbemba E, Marfaing R, Vaysse J, Pontet M, Saffar L, et al. Human alpha-fetoprotein binds to primary macrophages. *Biochem Biophys Res Commun.* 2002;296(3):507-14.
44. Dorr P, Westby M, Dobbs S, Griffin P, Irvine B, Macartney M, et al. Maraviroc (UK-427,857), a potent, orally bioavailable, and selective small-molecule inhibitor of chemokine receptor CCR5 with broad-spectrum anti-human immunodeficiency virus type 1 activity. *Antimicrob Agents Chemother.* 2005;49(11):4721-32.
45. Muraresku CC, McCormick EM, and Falk MJ. Mitochondrial Disease: Advances in clinical diagnosis, management, therapeutic development, and preventative strategies. *Curr Genet Med Rep.* 2018;6(2):62-72.
46. Spoor J, Farajifard H, and Rezaei N. Congenital neutropenia and primary immunodeficiency diseases. *Crit Rev Oncol Hematol.* 2019;133:149-62.
47. Waldmann TA, and McIntire KR. Serum-alpha-fetoprotein levels in patients with ataxia-telangiectasia. *Lancet.* 1972;2(7787):1112-5.
48. Renaud M, Tranchant C, Koenig M, and Anheim M. Autosomal Recessive Cerebellar Ataxias With Elevated Alpha-Fetoprotein: Uncommon Diseases, Common Biomarker. *Mov Disord.* 2020;35(12):2139-49.
49. Krumlauf R, Chapman VM, Hammer RE, Brinster R, and Tilghman SM. Differential expression of alpha-fetoprotein genes on the inactive X chromosome in extraembryonic and somatic tissues of a transgenic mouse line. *Nature.* 1986;319(6050):224-6.

50. Perincheri S, Dingle RW, Peterson ML, and Spear BT. Hereditary persistence of alpha-fetoprotein and H19 expression in liver of BALB/cJ mice is due to a retrovirus insertion in the Zhx2 gene. *Proc Natl Acad Sci U S A.* 2005;102(2):396-401.
51. Xie Z, Zhang H, Tsai W, Zhang Y, Du Y, Zhong J, et al. Zinc finger protein ZBTB20 is a key repressor of alpha-fetoprotein gene transcription in liver. *Proc Natl Acad Sci U S A.* 2008;105(31):10859-64.
52. Cobine PA, Moore SA, and Leary SC. Getting out what you put in: Copper in mitochondria and its impacts on human disease. *Biochim Biophys Acta Mol Cell Res.* 2021;1868(1):118867.
53. Baker ZN, Cobine PA, and Leary SC. The mitochondrion: a central architect of copper homeostasis. *Metallomics.* 2017;9(11):1501-12.
54. Leary SC, Cobine PA, Kaufman BA, Guercin GH, Mattman A, Palaty J, et al. The human cytochrome c oxidase assembly factors SCO1 and SCO2 have regulatory roles in the maintenance of cellular copper homeostasis. *Cell Metab.* 2007;5(1):9-20.
55. Leary SC, Cobine PA, Nishimura T, Verdijk RM, de Krijger R, de Coo R, et al. COX19 mediates the transduction of a mitochondrial redox signal from SCO1 that regulates ATP7A-mediated cellular copper efflux. *Mol Biol Cell.* 2013;24(6):683-91.
56. Hamza I, Prohaska J, and Gitlin JD. Essential role for Atox1 in the copper-mediated intracellular trafficking of the Menkes ATPase. *Proc Natl Acad Sci U S A.* 2003;100(3):1215-20.
57. Bull PC, Thomas GR, Rommens JM, Forbes JR, and Cox DW. The Wilson disease gene is a putative copper transporting P-type ATPase similar to the Menkes gene. *Nat Genet.* 1993;5(4):327-37.
58. Vulpe C, Levinson B, Whitney S, Packman S, and Gitschier J. Isolation of a candidate gene for Menkes disease and evidence that it encodes a copper-transporting ATPase. *Nat Genet.* 1993;3(1):7-13.
59. Schilsky ML. Wilson disease: Clinical manifestations, diagnosis, and treatment. *Clin Liver Dis (Hoboken).* 2014;3(5):104-7.
60. Davis RL, Liang C, and Sue CM. A comparison of current serum biomarkers as diagnostic indicators of mitochondrial diseases. *Neurology.* 2016;86(21):2010-5.
61. Koene S, de Laat P, van Tienoven DH, Weijers G, Vriens D, Sweep FC, et al. Serum GDF15 Levels Correlate to Mitochondrial Disease Severity and Myocardial Strain, but Not to Disease Progression in Adult m.3243A>G Carriers. *JIMD Rep.* 2015;24:69-81.
62. Yatsuga S, Fujita Y, Ishii A, Fukumoto Y, Arahata H, Kakuma T, et al. Growth differentiation factor 15 as a useful biomarker for mitochondrial disorders. *Ann Neurol.* 2015;78(5):814-23.
63. Forsstrom S, Jackson CB, Carroll CJ, Kuronen M, Pirinen E, Pradhan S, et al. Fibroblast Growth Factor 21 Drives Dynamics of Local and Systemic Stress Responses in Mitochondrial Myopathy with mtDNA Deletions. *Cell Metab.* 2019;30(6):1040-54 e7.
64. Kuhl I, Miranda M, Atanassov I, Kuznetsova I, Hinze Y, Mourier A, et al. Transcriptomic and proteomic landscape of mitochondrial dysfunction reveals secondary coenzyme Q deficiency in mammals. *Elife.* 2017;6.
65. Lehtonen JM, Auranen M, Darin N, Sofou K, Bindoff L, Hikmat O, et al. Diagnostic value of serum biomarkers FGF21 and GDF15 compared to muscle sample in mitochondrial disease. *J Inherit Metab Dis.* 2021;44(2):469-80.

66. Maresca A, Del Dotto V, Romagnoli M, La Morgia C, Di Vito L, Capristo M, et al. Expanding and validating the biomarkers for mitochondrial diseases. *J Mol Med (Berl).* 2020;98(10):1467-78.
67. Tyynismaa H, Carroll CJ, Raimundo N, Ahola-Erkkila S, Wenz T, Ruhanen H, et al. Mitochondrial myopathy induces a starvation-like response. *Hum Mol Genet.* 2010;19(20):3948-58.
68. Potting C, Tatsuta T, Konig T, Haag M, Wai T, Aaltonen MJ, et al. TRIAP1/PRELI complexes prevent apoptosis by mediating intramitochondrial transport of phosphatidic acid. *Cell Metab.* 2013;18(2):287-95.
69. Brunetti-Pierri N, and Ng P. Helper-dependent adenoviral vectors for liver-directed gene therapy. *Hum Mol Genet.* 2011;20(R1):R7-13.
70. Brunetti-Pierri N, Ng T, Iannitti D, Cioffi W, Stapleton G, Law M, et al. Transgene expression up to 7 years in nonhuman primates following hepatic transduction with helper-dependent adenoviral vectors. *Hum Gene Ther.* 2013;24(8):761-5.

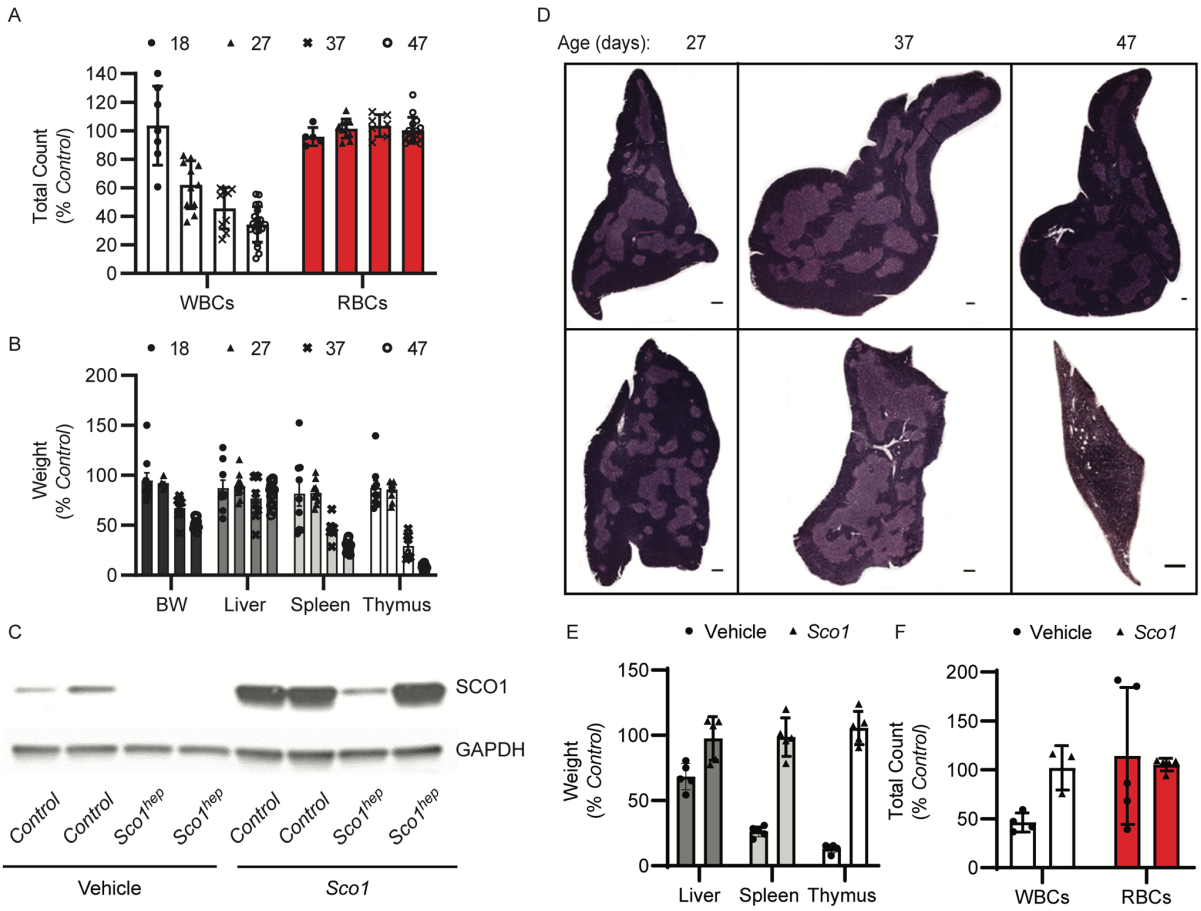

Figure 1: Ablation of *Sco1* expression in hepatocytes results in and unexpected reduction in circulating white blood cell counts and atrophy of the thymus and spleen.

A) Progressive leukopenia in $Sco1^{hep}$ mice (ANOVA, n=5-20; $p< 0.01$), *B)* disproportionate reduction in the wet weights of the $Sco1^{hep}$ spleen and thymus at P37 (t-test, n=8; $p<0.01$) and P47 (t-test, n=13; $p<0.001$) and *C)* selective thinning of the thymic cortex. Scale bars 2mm except for P47 $Sco1^{hep}$ thymus (800µm). *D)* Adenoviral restoration of SCO1 expression in the

liver leads to *E)* rescue of splenic and thymic atrophy (n=5) and *F)* normalization of WBC counts (n=3-5). Mice were injected at P21 via cardiac puncture with vehicle or helper-dependent adenovirus harbouring a *Sco1* cDNA under the control of a liver-specific promoter and harvested at P47. *Control* refers to wild-type littermates. BW refers to body weight. WBC and RBC denote white and red blood cells, respectively.

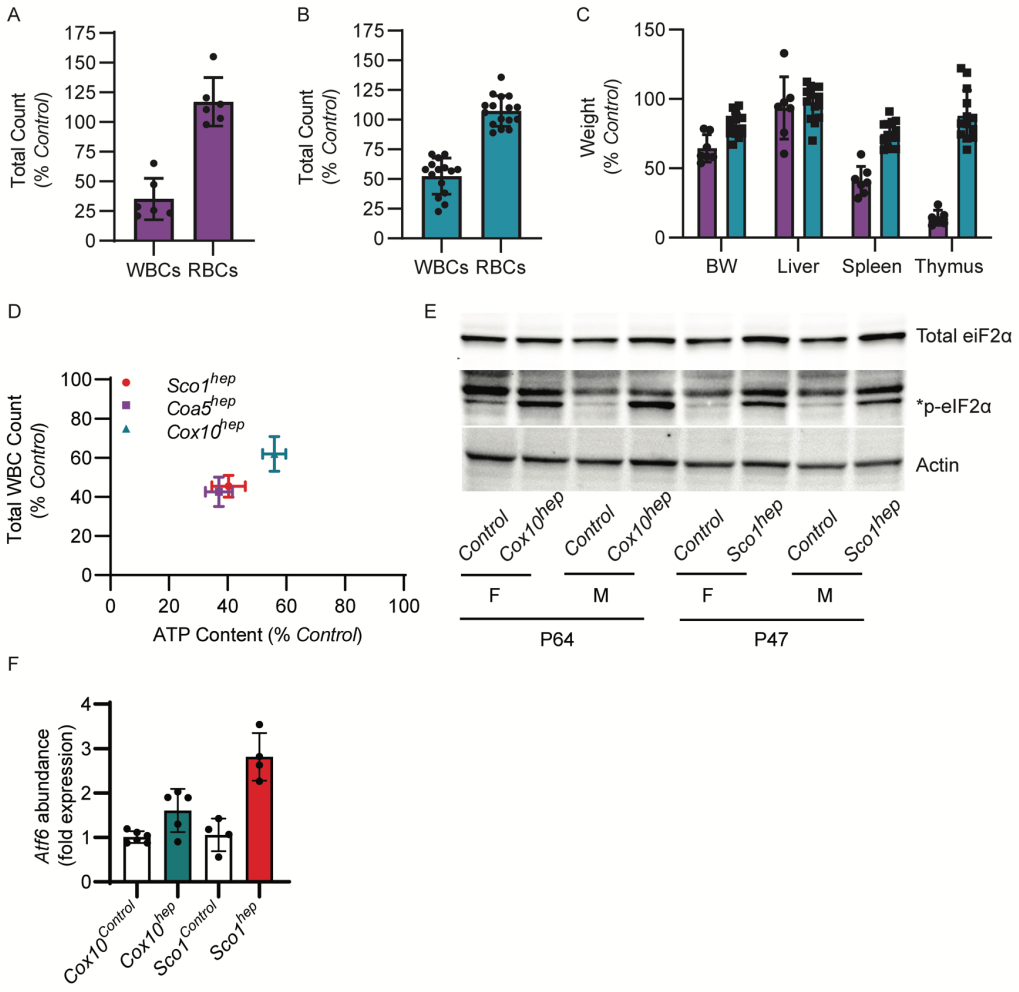

Figure 2. The reduction in peripheral white blood cell counts in hepatocytes is positively correlated with the bioenergetic deficit in the liver.

A) Coa5^{hep} (t-test, n=6; p<0.001) and *B) Cox10*^{hep} (t-test, n=15-16; p<0.01) mice also exhibit a significant leukopenia. *C) Coa5*^{hep} mice have a disproportionate reduction in the wet weight of the spleen (t-test, n=6; p<0.01) and thymus (t-test, n=5; p<0.001), while *Cox10*^{hep} mice exhibit significant yet milder atrophy of the spleen (t-test, n=14; p<0.05). *D)* Total WBC counts are

positively correlated with liver ATP content in all three *hep* mouse models (linear regression R^2= 0.99; p=0.001). P47 *Sco1*^{hep} and P64 *Cox10*^{hep} livers have higher levels of *E)* the phosphorylated form of eIF2α, an ISR marker, and *F)* the *Atf6* transcript, a marker of ER stress (ANOVA, n=4-6; p<0.005, *Sco1*^{hep} model; p<0.02; *Cox10*^{hep} model).

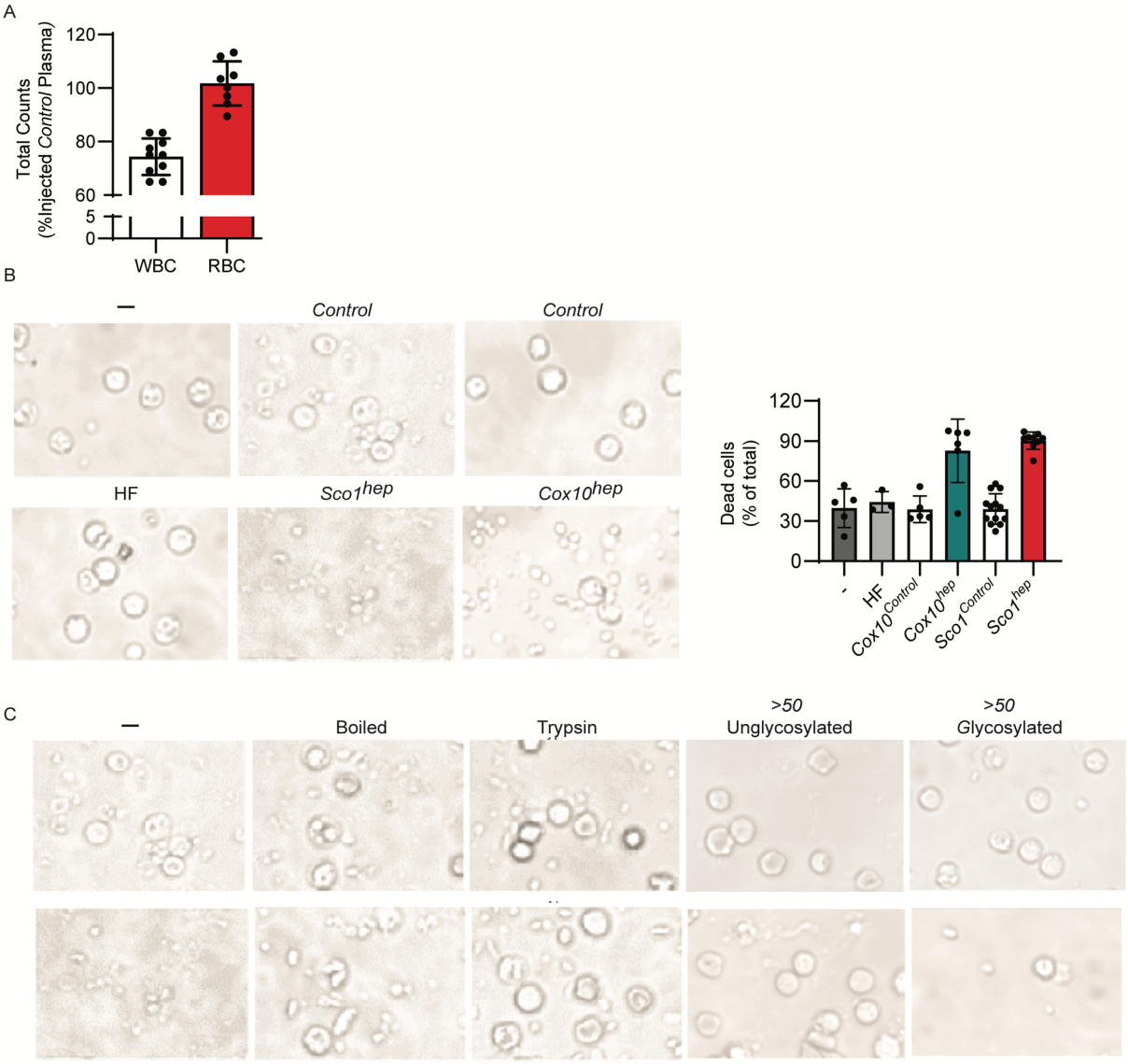

Figure 3: A glycoprotein secreted by mice with altered mitochondrial function in the liver is responsible for the observed reduction in peripheral white blood cell counts.

A) Total WBC counts are reduced in *Control* mice injected with *Sco1*^{hep} plasma relative to those injected with *Control* plasma (t-test, n=10; p=0.02). *B)* The viability of PBMCs isolated from *Control* mice is significantly reduced when they are co-cultured with *Sco1*^{hep} or *Cox10*^{hep} plasma. PBMC viability is unaffected by exposure to plasma from mice fed a high fat (H*F*) diet. Bar graph

on right hand side summarizes the operator-blinded quantitation of dead cells per treatment group expressed as a percentage of the total number of cells (live and dead) per image (n=3-13 per treatment group, $p<0.0001$, both *hep* models versus –, HF or *Control* treatments). *C)* PBMC viability is rescued if $Sco1^{hep}$ plasma is boiled or treated with trypsin. Fractionation based on size and the presence of a glycan revealed that the factor(s) that reduces PBMC viability is contained in a >50kDa glycoprotein fraction. For *B)* and *C)* all images are 50μm in scale, and the – denotes PBMCs cultured in FBS alone. The *Control* and $Sco1^{hep}$ images in panel *B*) are identical to those denoted as – in panel *C*) because they were part of the same experimental series.

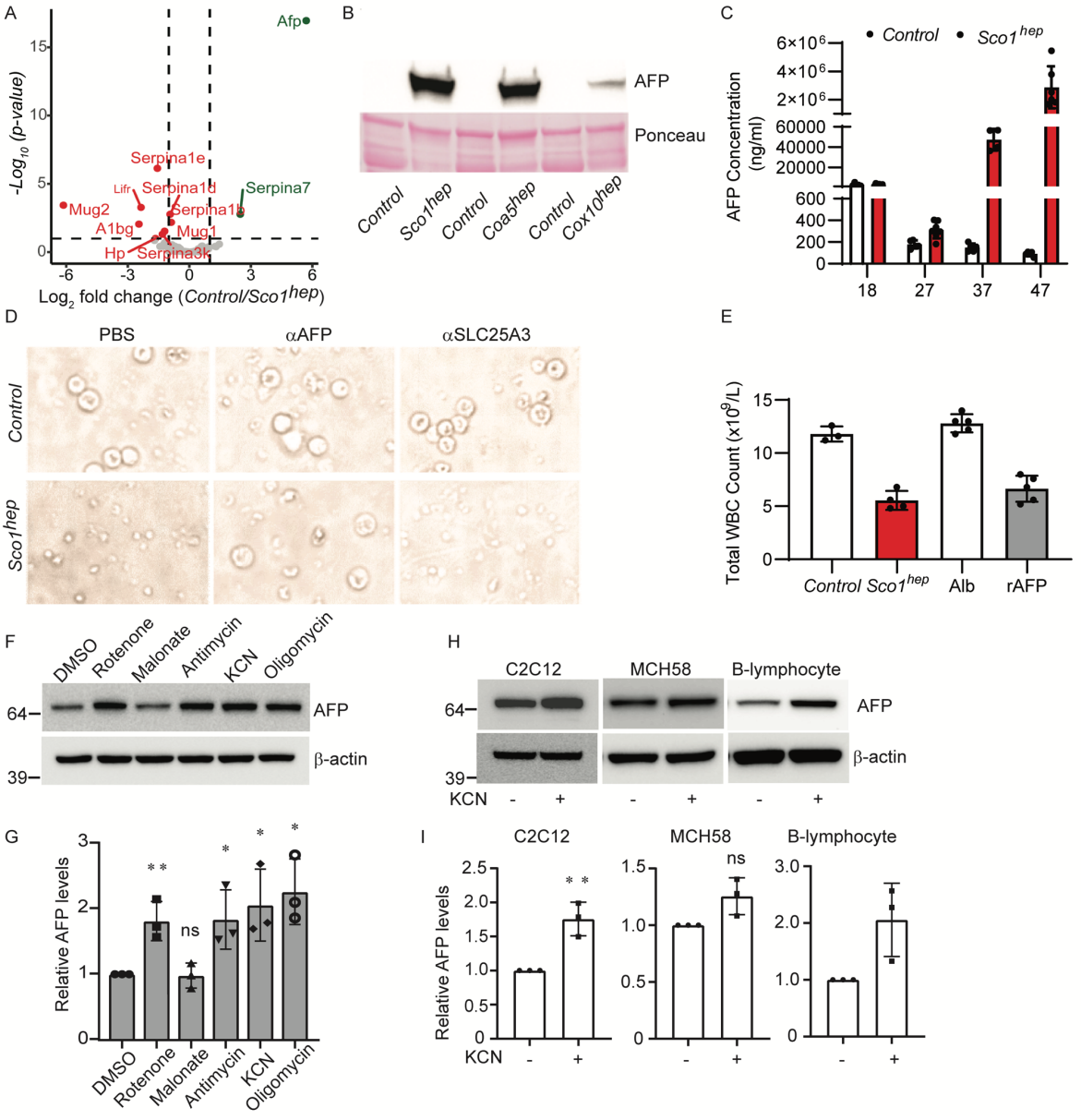

Figure 4: AFP expression is increased in response to impaired organelle function and is directly responsible for the leukopenia observed in several mitochondrial disease models.

A) AFP is significantly enriched in *hep* relative to *Control* plasma. Volcano plot with dotted lines indicating a 2-fold change and adjusted p-value significance threshold of 0.1. A green or red symbol indicates a protein whose abundance is significantly up- or down-regulated, respectively. Grey symbols denote proteins whose abundance is not significantly different (ns) between the two groups. *B)* AFP abundance is markedly upregulated in *Sco1*^{hep}, *Coa5*^{hep} and *Cox10*^{hep} plasma.

Plasma was pooled (minimum of two males and two females per pool) and depleted of immunoglobulins and albumin prior to Western blotting. The Ponceau stained membrane indicates relative loading across lanes. *C)* AFP progressively accumulates in *Sco1*^{hep} plasma (t-test (n=4-7); P27, $p< 0.05$, P37, $p< 0.0001$, P47, $p< 0.0001$). *D)* PBMC viability is rescued by immunodepleting AFP from *Sco1*^{hep} plasma. Culture media supplemented with phosphate buffered saline (PBS) and plasma incubated with αSLC25A3, an antibody isotype control, served as internal controls. *E) Control* mice develop a leukopenia following serial injection with *Sco1*^{hep} plasma (t-test, n=3-4; $p<0.01$) or 1μg of recombinant AFP (rAFP) (t-test, n=5; $p<0.01$). *Control* mice injected with *Control* plasma or albumin served as internal controls. *F&G)* Inhibition of the mitochondrial respiratory chain elevates AFP abundance in C2C12 myoblasts. *H&I)* AFP levels increase in C2C12 myoblasts and human B-lymphoblasts upon inhibition of COX For panels *F-I)* β-actin was used as a loading conrol and data are shown as mean ± SD, n=3. *$p < 0.05$, **$p < 0.005$. ns, not significant. **$p < 0.005$.

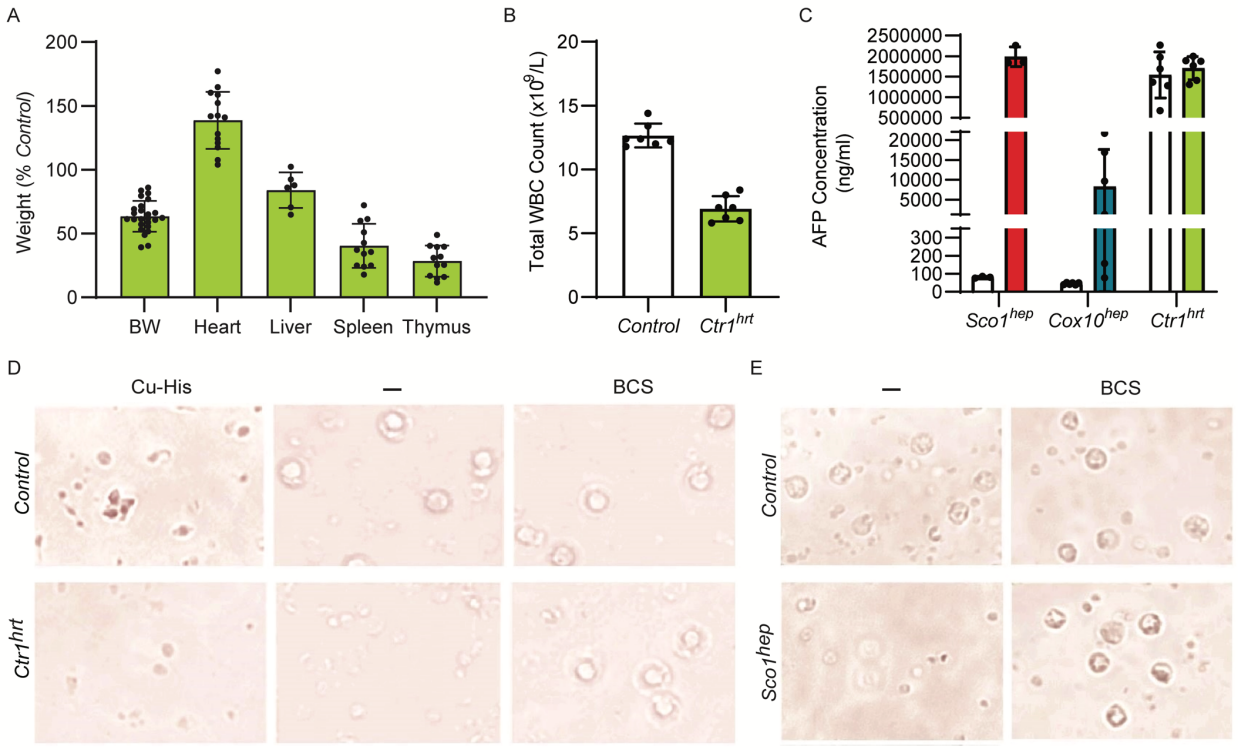

Figure 5: AFP requires copper to promote the death of peripheral white blood cells.

A&B) Ctr1^{hrt} mice exhibit disproportionate atrophy of the spleen (t-test, n=12; p<0.01) and thymus (t-test, n=12; p< 0.01) and have a *B)* leukopenia (t-test, n=7; p< 0.01). *C)* Plasma AFP levels are comparable in P10 *Control* and *Ctr1*^{hrt} plasma mice. Relative levels of AFP in *Sco1*^{hep}, *Cox10*^{hep} age-matched littermate *Control* plasma were quantified at the same time and are shown here for comparative purposes (n=3-6). *D)* PBMC viability is adversely affected by *Ctr1*^{hrt}

plasma, an effect that can be rescued by adding the copper chelator bathocuproine sulphonate (BCS) to the media. Viability of PBMCs is also reduced if copper-histidine (Cu-His) is added to media containing P10 *Control* plasma. *E)* BCS also negates the negative effect of *Sco1*^{hep} plasma on PBMC viability. For *D)* and *E)* all images are 50μm in scale.

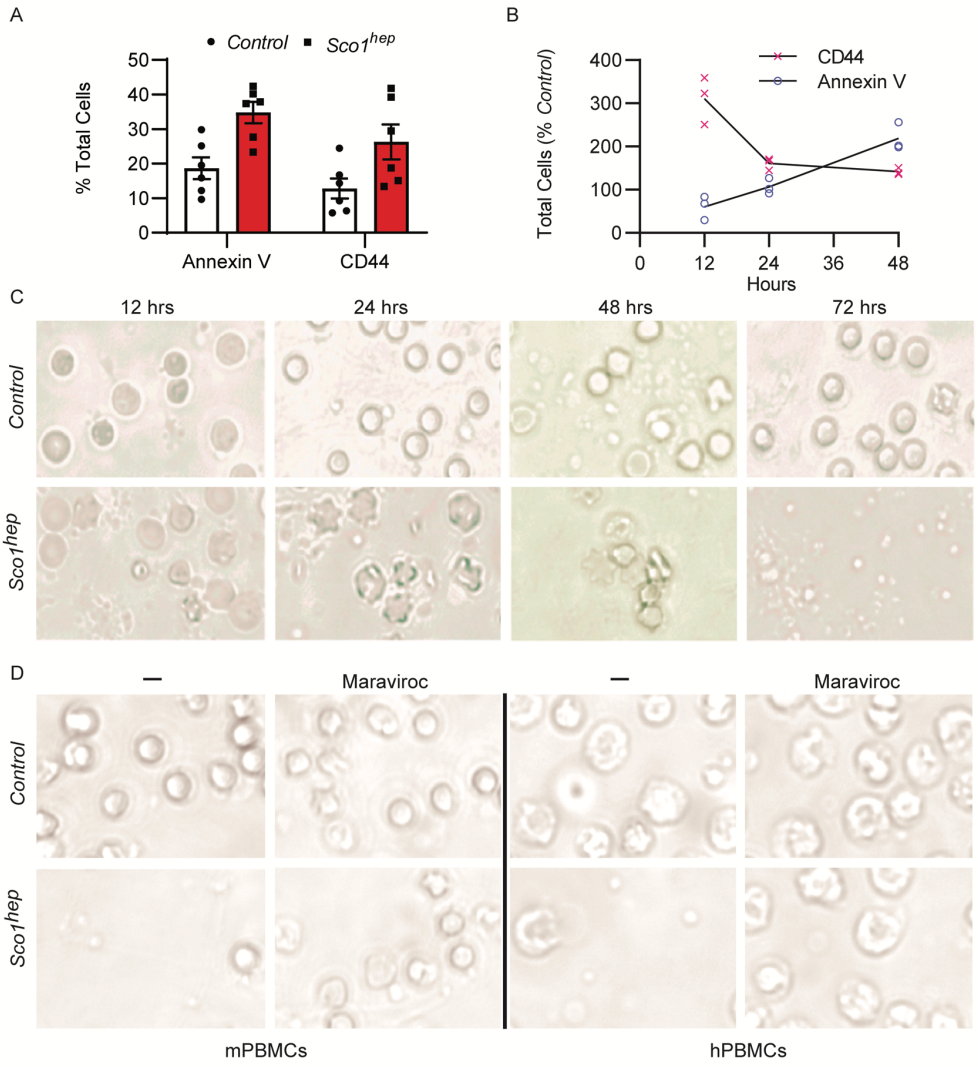

Figure 6: AFP promotes activation and apoptosis of both mouse and human white blood cells via the cell surface receptor CCR5.

PBMCs isolated from peripheral blood of *Sco1*^{hep} mice have an increased number of cells that stain positive for the activation marker CD44 and the apoptotic marker Annexin V when compared to PBMCs isolated from *Controls* (n=6). *B)* PBMCs isolated from *Control* mice were co-cultured in media containing *Sco1*^{hep} plasma are activated earlier and demonstrate a

progressive increase in cell surface expression of the apoptotic marker annexin V relative to PBMCs cultured in *Control* plasma (n=3). *C)* Cells analyzed in *B)* show blebbing (a sign of apoptosis) as early as 12-24 hrs in culture and loss of cellularity after 72 hr in culture in response to co-culture with $Sco1^{hep}$ but not *Control* plasma. *D)* Human PBMC viability is also reduced in media containing $Sco1^{hep}$ plasma, and can be rescued with the CCR5 antagonist Maraviroc. mPBMCs and hPBMCs denote PBMCs of mouse or human origina, respectively (mPBMCs, n=3; hPBMCs n=2; each replicate contained a triplicate for each experimental condition). For *C)* and *D)* all images are 50μm in scale.

Table 1. Description, details and origin of key resources used in this study.

Reagent or Resource	Source	Identifier
Antibodies		
SCO1	Rabbit polyclonal	In-house
GAPDH	Cell Signaling	2118
ATP7A	In-house	(18)
CTR1	GenScript	In-house
eIF2α	Cell Signaling	9722
phospho-eIF2α	Cell Signaling	9721
Actin hFAB rhodamine	Cell Signaling	12004163
SD70	Mitoscience	MS204
Core 1	Mitoscience	MS303
ATP5A	Abcam	Ab14748
NDUFA9	Mitoscience	MS111
COX1	Mitoscience	MS404
COX4	Mitoscience	MS407
TOM40	Proteintech	18409-1-AP
AFP	Abcam	Ab46799
Tubulin	Santa Cruz	sc-5286
CD16/CD32 (Fc Block)	BD Biosciences	553141
CD3	BD Biosciences	565643
CD4	BD Biosciences	557308
CD8	BD Biosciences	553030

CD25	BD Biosciences	552880
CD44	BD Biosciences	563736
CD69	BD Biosciences	561240
FITC Annexin V	BD Biosciences	556419
Annexin V Binding Buffer, 10X	BD Biosciences	556454
Bacterial and Virus Strains		
XL1-Blue Competent Cells	Agilent	200249
HDΔ28E4LacZ	In-house	(69, 70)
HDΔ24.7E4-pepck-mSCO1	In-house	(69, 70)
Chemicals, Peptides, and Recombinant Proteins		
Ammonium persulfate	BioShop	AMP001.100
Acrylamide	Sigma	A8887-500G
Bathocuproinedisulfonic acid disodium salt	Sigma	B1125-1G
Calcium chloride dihydrate	EM Science	B10070-34
Cupric chloride dihydrate	BioShop	CUC002.100
Cupric sulfate pentahydrate	Sigma	C-8027
Dimethyl sulfoxide	BioShop	DMS666.50
Ethylenediamine	BioShop	EDT001.500
Ethylenediamine tetraacetic acid dipotassium salt dihydrate	Fisher	BP19-500
Glycine	BioShop	GLN002.5
L-Histidine	Sigma	H9288

Maraviroc	Sigma	PZ0002
PMSF	BioShop	PMS123.5
Potassium chloride	EM Science	PX1405-1
SDS	BioShop	SDS001.1
Sodium chloride	BioShop	SOD002.5
Potassium phosphate, monobasic	BioShop	PPM302.500
Sodium phosphate, dibasic	BioShop	SPD579.1
Triton-X 100	BioShop	TRX777.5
Tween-20	Fisher	BP337-500
Trypan blue solution (0.4%)	Sigma	T8154
Tris	BioShop	TRS001.5
Skim Milk (Blotto)	US Biological	S1013-90A
TEMED	BioShop	TEM001.5
Complete Protease Inhibitor Cocktail (PIC)	Roche	11 836 145 001
Hydrogen peroxide solution	Sigma	216763
Albumin (Bovine)	BioShop	ALB001.500
Dithiotreitol (DTT)	Fisher	BP172-5
Oxaloacetic acid (OAA)	Sigma	O4126-1G
Proteinase K from *Tritirschium album*	Sigma	P2308-100MG
Cytochrome *c*	Sigma	C-7752
Agarose	BioShop	AGA002.1

SYBR Safe DNA gel stain	Invitrogen	S33102
Generuler (100bp)	Thermo	SM0241
p-Coumaric acid	Sigma	C9008-5G
Luminol	Sigma	A8511-5G
Ponceau S	Fisher	40058003755
Recombinant Mouse α-fetoprotein (AFP)	Mybiosource	MBS717717
Trichloroacetic acid (TCA)	Sigma	T0699
RPMI 1640 Medium	GE	SH30096.01
10X PBS	Fisher	BP3994
FBS	Gibco	12483020
Recombinant human interleukin-2 (IL-2)	Stem Cell	78036.3
Ficoll Paque Plus	Sigma	17-1440-02
Hank's Balanced Salt Solution (HBSS) (10X)	Gibco	14065056
Isoflurane	Fresenius Kabi	CP0406V2
Harris Hematoxylin	Leica	3801562
Eosin Y	Leica	3801602
Critical Commercial Assays		
Phire Animal Tissue Direct PCR kit	Thermo	#F-140WH
Mouse AFP Quantikine ELISA Kit	R&D Systems	MAFP00
ENLITEN® ATP Assay System Bioluminescence Detection Kit for ATP Measurement	Promega	FF2000
Qproteome Total Glycoprotein Kit	Qiagen	37541

Experimental Models: *Mouse strains*		
Alb-cre	Jax	#003574
Sco1	In-house	(18)
Coa5	KOMP - ES cells; Toronto Centre for Phenogenomics - mice	
Cox10	Jax	#024697
Ctr1	In-house	(34)
Cell lines		
MCH58 human skin fibroblasts	Dr. Eric Shoubridge, McGill University	
C2C12 murine myoblasts	Dr. Miriam L. Greenberg, Wayne State University	
Control B-lymphocytes	Coriell Institute	ND11500
Oligonucleotides		
Sco1-F ATGGAATCCCTTCCTTGCTTC	In-house	(18)
Sco1-R1 TCAACCTCAACATTTCACGACGGTATT	In-house	(18)
Sco1-R2	In-house	(18)

ACCTAAAAGTGGGGCTTCCTGAAAACTAA		
Cox10-F GAGAGGAGTCAAGGGGACCT	This study	N/A
Cox10-R1 GGCCTGCAGCTCAAAGTGTA	This study	N/A
Cox10-R2 CAAAGAGGGCTCACTTCTTGC	This study	N/A
Coa5-F GAGCTCTCATGCACAGCAAG	This study	N/A
Coa5-R1 TTCAAGTCGTGGAATGGTAGC	This study	N/A
Coa5-R2 GCTGCTAGGACCAAATCCTG	This study	N/A
Ctr1-P1 AATGTCCTGGTGCGTCTGAAA	In-house	(34)
Ctr1-P2 GCAGTAGATAAAAGCCAAGGC-30	In-house	(34)
Ctr1-P3 AAAAACCACTATTCAGAGACTG	In-house	(34)
Afp-F AGTTGCAAAGCACATGAAGA	IDT	
Afp-R AAGCACTCCTCCTTGTTGTC	IDT	
Gapdh-F	IDT	

CATGGCCTTCCGTGTTCCTA		
Gapdh-R CCTGCTTCACCACCTTCTTGA	IDT	
ATF6-F TCGCCTTTTAGTCCGGTTCTT	IDT	
ATF6-R GGCTCCATAGGTCTGACTCC	IDT	
Software & Algorithms		
GraphPad Prism 8.0/9.0		
CytExpert		
ImageJ		